A New Rotor-Ball Bearing-Stator Coupling Dynamics Model for Whole Aero-Engine Vibration

G. Chen
College of Civil Aviation,
Nanjing University of Aeronautics and Astronautics,
Nanjing, 210016, P. R. China
e-mail: cgzyx@263.net

In this paper, a new rotor-ball bearing-stator coupling system dynamics model is established for simulating the practical whole aero-engine vibration. The main characteristics of the new model are as follows: (1) the coupling effect between rotor, ball bearing, and stator is fully considered; (2) the elastic support and the squeeze film damper are considered; (3) the rotor is considered as an Euler free beam of equal-section model, and its vibration is analyzed through truncating limited modes; (4) nonlinear factors of ball bearing such as the clearance of bearing, nonlinear Hertzian contact force, and the varying compliance vibration are modeled; and (5) rubbing fault between rotor and stator is considered. The Zhai method, which is a new explicit fast numerical integration method, is employed to obtain system's responses, and the whole aero-engine vibration characteristics are studied. Finally, aero-engine tester including casing is established to carry out rubbing fault experiment, the simulation results from rotor-ball bearing-stator coupling model are compared with the experiment results, and the correctness of the new model is verified to some extent. [DOI: 10.1115/1.4000475]

1 Introduction

In general, the rotor of aero-engine is supported on the stator casing through bearing, and the casing is installed on a base or is suspended on the aircraft. The elastic support and the squeeze film damper (SFD) are often designed between bearings and bearing housing in order to reduce the vibration of rotor and adjust the critical speeds of rotor. Therefore, it is clearly known that their motions are coupled to each other, and a rotor-ball bearing-stator coupling system is formed in the perspective of structure and dynamics. With the aero-engine performance continuously improving, we are always trying to modify the geometry of components in order to greatly increase thrust weight ratio and structural efficiency, which can make full use of the material properties. Narrowing the clearance between rotor and stator is one of the important measures, but the disadvantage is that probability of the rotor/stator rub-impact increases greatly. The rotor/stator rub-impact faults may result in many serious consequences such as magnifying the clearance between rotor and stator, wearing bearings, breaking blades, and even resulting in mechanical failure. Therefore, at present, many scholars have done further researches on rubbing [1,2]. Usually, rub-impact faults are secondary faults with apparent coupling faults' characteristics, which result from the imbalance, misalignment, pedestal looseness, oil whirl, and oil oscillation, and now, the research on coupling faults of rub and impact has gradually become a new focus [3,4]. Presently, all of the bearing models on coupling multifaults including rub-impact faults are almost sliding bearing; however, rolling bearing is commonly used in aero-engine; therefore, it is of great significance to model the rolling bearing in detail. In recent years, researches have been advanced, and many dynamic models including rub-impact faults in which rolling bearings are adopted, and many valuable conclusions have been obtained [5–9].

However, the above researches all adopt the simple Jeffcott rotor model, which are too simple to simulate practical rotor vibration. As to researches on the actual rotor system, transfer matrix method and finite element (FE) method are the main methods, and the transfer matrix method is the most popular method to the rotor system with a chain structure. Transfer matrix method, in essence, is a method based on discrete rotor model, and it has been a relatively mature theory and method at the aspect of the calculation of critical speeds and simple unbalance responses of complex rotor system; however, it is very difficult to calculate strongly nonlinear response for rotor system with faults and obtain satisfactory results; in addition, the transfer matrices are not suited for modeling complex subsystems such as the engine casing; for this reason, the transfer matrix approach has not crossed over the whole-engine modeling [10]. Finite element method can be also applied in rotor dynamics analysis, but when dealing with large-order systems, the direct integration of the FE equations is highly time-consuming and so is generally avoided [10,11], additionally, the FE method is difficult to deal with nonlinear problem too, and it needs to combine with the other methods [9,10].

To sum up, Jeffcott rotor model can be used to solve strongly nonlinear rotor dynamics problems, but there is a great difference between Jeffcott rotor model and the actual one. The transfer matrix method and the FE method are highly time-consuming and very difficult to deal with the nonlinear problem of the complex large-scale rotor-ball bearing-stator coupling system. In view of this case, in this paper, a new rotor dynamics model is established, in which rotor is considered as an Euler free beam of equal-section model, bearing force is imposed on the two ends of rotor in the way of concentrated force, the concentrated binding force can also help to connect disk and rotor shaft, and rotor response can be obtained through modal truncation method in this paper. A new dynamic model for rotor-ball bearing-stator coupling system for whole aero-engine vibration is established based on the new rotor dynamics model, in which the coupling effect between rotor, ball bearing, and stator is fully considered, and the Hertzian nonlinear contact force and varying compliance (VC) vibration of ball bearing, and rub-impact effect between rotor and stator are also taken into account. The nonlinear responses of the system are acquired by means of numerical integration method, and some whole aero-engine vibration characteristics are studied. Finally, experimental verification is carried out by an aero-engine rotor tester.

Contributed by the Technical Committee on Vibration and Sound of ASME for publication in the JOURNAL OF VIBRATION AND ACOUSTICS. Manuscript received September 25, 2008; final manuscript received July 29, 2009; published online November 19, 2009. Assoc. Editor: Kon-Well Wang.

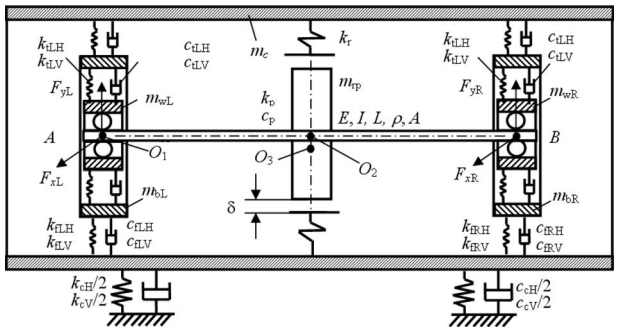

Fig. 1 The new rotor-ball bearing-stator coupling dynamics model with rubbing fault

2 The New Rotor-Ball Bearing-Stator Coupling Dynamics Model for Whole-Engine Vibration

2.1 Schematic of the New Model. The new dynamic model for rotor-ball bearing-stator coupling system for whole-engine vibration is shown in Fig. 1, at the two ends of which there are two same rolling bearings. When rotor rotating, great transverse bending vibration may be caused due to the excitation of imbalance fault, and when the amplitude of vibration exceeds the clearance between rotor and stator, rotor-stator rubbing fault appears.

The symbols in Fig. 1 are illustrated as follows: m_c is the mass of stator; m_{rp} is the mass of disk; m_{wL} and m_{wR} are the masses of the left and right rolling bearing outer-rings; m_{bL} and m_{bR} are the masses of the left and right bearing housings; E, I, L, ρ, and A are the elastic modulus, inertia moments, length, density, and sectional area of the rotating shaft; k_r is the rubbing contact stiffness; k_p and c_p are the connection stiffness and damping between rotating shaft and disk; k_{tLH} and k_{tLV} are the horizontal and vertical elastic support stiffnesses between left rolling bearing outer-ring and left bearing housing; c_{tLH} and c_{tLV} are the horizontal and vertical dampings between left rolling bearing outer-ring and left bearing housing (here nonlinear SFD is considered); k_{tRH} and k_{tRV} are the horizontal and vertical elastic support stiffnesses between right rolling bearing outer-ring and right bearing housing; c_{tRH} and c_{tRV} are the horizontal and vertical dampings between right rolling bearing outer-ring and right bearing housing (here nonlinear SFD is considered); k_{fLH} and k_{fLV} are the horizontal and vertical support stiffnesses between stator and left bearing housing; c_{fLH} and c_{fLV} are the horizontal and vertical support dampings between stator and left bearing housing; k_{fRH} and k_{fRV} are the horizontal and vertical support stiffnesses between stator and right bearing housing; c_{fRH} and c_{fRV} are the horizontal and vertical support dampings between stator and right bearing housing; k_{cH} and k_{cV} are the horizontal and vertical support stiffnesses between stator casing and base; c_{cH} and c_{cV} are the horizontal and vertical support dampings between stator and base; O_1, O_2, and O_3 are the geometric center of bearing, geometric center of rotor, and centroid of rotor; δ is the clearance between disk and stator; e is the eccentricity distance; F_{xbL} and F_{ybL} are the supporting force components in the X and Y directions of the left bearing; F_{xbR} and F_{ybR} are the supporting force components in the X and Y directions of the right bearing; and P_T and P_N are the tangential component and normal component of the rub-impact force.

2.2 Differential Equations of Motion for New Model

2.2.1 Rotor Dynamics Model Based on Free Euler Beam of Equal-Section. The rotor analysis model is Euler free beam of equal-section model, and it is shown in Fig. 2. F_{xp} and F_{yp}, respectively, represent the concentrated forces of disk to shaft in the X and Y directions. F_{xbL} and F_{ybL}, respectively, represent the concentrated forces of the left bearings to shaft in the X and Y directions. F_{xbR} and F_{ybR}, respectively, represent the acting force of the right bearings to shaft in the x and y directions. L represents the length of the shaft. The rotor model in this paper is assumed symmetrical to the central plane and the gyroscopic forces are neglected. The coordinate system o-xyz is the one fixed at the left end of he shaft, in which transverse bending vibrations in oyz and oxz coordinate planes are considered in this model.

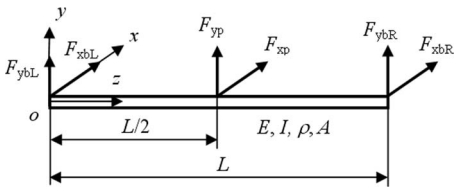

Fig. 2 Rotor model based on Euler free beam of equal-section

2.2.1.1 Transverse bending vibrations in oxz coordinate plane. The vibration displacement of shaft in the oxz plane is represented as $x_r(z,t)$, and elastic modulus, inertia moments, density, and sectional area of the rotating shaft are, respectively, represented as E, I, ρ, and A; thus, the differential equation of vibration for the shaft can be expressed as

$$EI\frac{\partial^4 x_r(z,t)}{\partial z^4} + \rho A\frac{\partial^2 x_r(z,t)}{\partial^2 t} = F_{xbL}\delta(z) + F_{xbR}\delta(z-L) + F_{xp}\delta(z-L/2) \quad (1)$$

where $F_{xp}=k_p[x_p(t)-x_r(L/2,t)]+c_p[\dot{x}_p(t)-\dot{x}_r(L/2,t)]$, F_{xbL} and F_{xbR}, respectively, represent the left and right bearing forces, and $x_p(t)$ is the vibration displacement of the rotor disk in the X direction. Equation (1) is a four-order partial differential equation, which needs to be transformed into two-order ordinary differential equations in order to conduct numerical analysis. The vibration of beam mainly depends on a few low-order vibration modals; therefore, the NM low-order modals are chosen to study the vibration of free beam with modal truncation method, and the orthogonal function system X_n $(n=1\sim NM)$ of the free Euler beam of equal-section is introduced [12], namely,

$$X_1 = 1$$

$$X_2 = \sqrt{3}(1-2z/L)$$

$$X_m = (ch\beta_m z + \cos\beta_m z) - C_m(sh\beta_m z + \sin\beta_m z), \quad m > 2 \quad (2)$$

where C_m and β_m are constants, and the values of C_m and $\beta_m L$ are shown in Table 1.

The transverse bending vibration of shaft in the oxz plane can be approximately expressed as

$$x_r(z,t) = \sum_{n=1}^{NM} X_n(z)T_{xn}(t) \quad (3)$$

A new equation is obtained by substituting formula (3) into formula (1). By multiplying $X_p(z)$, $p=1,2,\ldots,NM$ and then doing integral operation on z in the range of shaft full-length, we can get the following equation according to the modals' orthogonality and the properties of δ function:

Table 1 Coefficients for free beam functions

m	1	2	3	4	5	≥6
C_m	—	—	0.982502	1.000777	0.999966	1.000000
$\beta_m L$	0	0	4.730040	7.853200	10.99560	$(2m-3)\pi/2$

$$\rho A\ddot{T}_{xn}(t)\int_0^L X_n^2(z)dz + EIT_{xn}(t)\int_0^L X_n(z)\cdot\frac{d^4X_n(z)}{dz^4}dz = F_{xbL}X_n(0) + F_{xbR}X_n(L) + F_{xp}X_n(L/2) \quad (4)$$

Because of $\int_0^L X_n^2(z)dz = L$, $\int_0^L X_n(z)\cdot(d^4X_n(z)/dz^4)dz = L\cdot\beta_n^4$, formula (4) can be simplified as

$$\ddot{T}_{xn}(t) + \frac{EI\beta_n^4}{\rho A}T_{xn}(t) = \frac{F_{xbL}}{\rho AL}X_n(0) + \frac{F_{xbR}}{\rho AL}X_n(L) + \frac{F_{xp}}{\rho AL}X_n(L/2) \quad (5)$$

That is the basic form for the two-order ordinary differential equations ($n=1\sim NM$) in modal coordinates of shaft vibration in the oxz plane.

2.2.1.2 Transverse bending vibrations in oyz coordinate plane. The vibration displacement of shaft in the oyz plane is represented as $y_r(z,t)$, and the differential equation of vibration for the shaft can be expressed as

$$EI\frac{\partial^4 y_r(z,t)}{\partial z^4} + \rho A\frac{\partial^2 y_r(z,t)}{\partial^2 t} = F_{ybL}\delta(z) + F_{ybR}\delta(z-L) + F_{yp}\delta(z-L/2) + \rho A\cdot g \quad (6)$$

where $F_{yp}=k_p[y_p(t)-y_r(L/2,t)]+c_p[\dot{y}_p(t)-\dot{y}_r(L/2,t)]$, and F_{ybL} and F_{ybR}, respectively, represent the left and right bearing forces. $y_p(t)$ is the vibration displacement of the rotor disk in the y direction. Likewise, the NM low-order modals are chosen to study the vibration of free beam by means of modal truncation method, and the orthogonal function system Y_n $(n=1\sim NM)$ is

$$Y_1 = 1$$

$$Y_2 = \sqrt{3}(1-2z/L)$$

$$Y_m = (ch\beta_m z + \cos\beta_m z) - C_m(sh\beta_m z + \sin\beta_m z), \quad m>2 \quad (7)$$

where the values of C_m and $\beta_m L$ are shown in Table 1; thus the transverse bending vibration shaft in the oyz plane can be approximately expressed as

$$y_r(z,t) = \sum_{n=1}^{NM} Y_n(z)T_{yn}(t) \quad (8)$$

That is the basic form for the two-order ordinary differential equations ($n=1\sim NM$) in modal coordinates of shaft vibration in the oyz plane.

$$\ddot{T}_{yn}(t) + \frac{EI\beta_n^4}{\rho A}T_{yn}(t) = \frac{F_{ybL}}{\rho AL}Y_n(0) + \frac{F_{ybR}}{\rho AL}Y_n(L) + \frac{F_{yp}}{\rho AL}Y_n(L/2) + \frac{\rho A\cdot g}{\rho AL}\int_0^L Y_n(z)dz \quad (9)$$

2.2.2 Dynamic Equations for Rotor Disk. Disk and shaft are connected through the stiffness k_p and damping c_p in the X and Y directions in this model. The unbalanced force resulted from mass eccentricity and the rubbing between stator and rotor are considered, and the motion differential equation can be obtained according to Newton's second law.

$$m_{rp}\ddot{x}_{rp} + k_p[x_p(t)-x_r(L/2,t)] + c_p[\dot{x}_p(t)-\dot{x}_r(L/2,t)] = P_x + m_{rp}e\omega^2\cos(\omega t) \quad (10)$$

$$m_{rp}\ddot{y}_{rp} + k_p[y_p(t)-y_r(L/2,t)] + c_p[\dot{y}_p(t)-\dot{y}_r(L/2,t)] = P_y + m_{rp}e\omega^2\sin(\omega t) - m_{rp}g \quad (11)$$

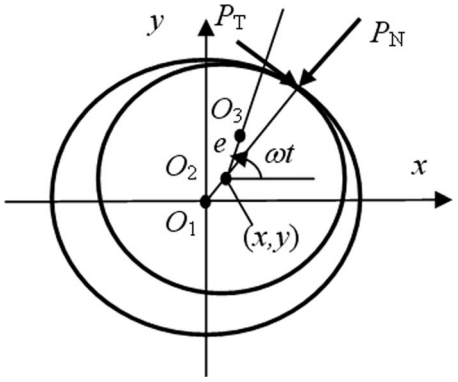

Fig. 3 Rub-impact model

2.2.3 Rotor-Stator Rubbing Model. The relative radical displacement between rotor and stator is represented as $r=\sqrt{(x_p-x_c)^2+(y_p-y_c)^2}$; when $r<\delta$, rubbing does not happen; that is, $P_x=P_y=0$; when $r\geq\delta$, rubbing happens (see Fig. 3). Assume the friction force conforms to the Coulomb friction law, then

$$P_N = k_r\cdot(e-\delta)$$

$$P_T = f\cdot P_N \quad (12)$$

where k_r is the radical stiffness of stator and f is the friction coefficient. Therefore, the components of rubbing force in the X and Y directions are

$$P_x = k_r(1-\delta/r)[-(x_p-x_c)+f\cdot(y_p-y_c)]$$

$$P_y = k_r(1-\delta/r)[-(y_p-y_c)-f\cdot(x_p-x_c)] \quad (13)$$

2.2.4 Ball Bearing Model. As shown in Fig. 4, the rolling bearing model considered here has equispaced balls rolling on the surfaces of the inner and outer races, and there is pure rolling of balls on the races so that the two points of the ball touching the outer and inner races have different linear velocities. It is assumed that v_{out} is the linear velocity of the point of ball touching the outer race, v_{in} is the linear velocity of the point of ball touching the inner race, ω_{out} is the rotational angular velocity of the bearing outer-ring, ω_{in} is the rotational angular velocity of the bearing inner-ring, R is the radius of the outer race, and r is the radius of the inner race; thus,

$$v_{out} = \omega_{out}\times R, \quad v_{in} = \omega_{in}\times r$$

The linear velocity of cage, that is, the linear velocity of the balls' center, can be expressed by $v_{cage}=(v_{out}+v_{in})/2$. In this pa-

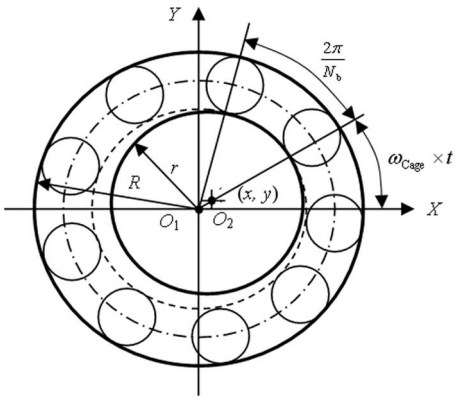

Fig. 4 Ball bearing model

per, it is assumed that the outer-ring is fixed rigidly and the inner-ring rotates with the shaft; thus, $v_{out}=0$, $v_{cage}=v_{in}/2=(\omega_{in}\times r)/2$, and the angular velocity of cage is

$$\omega_{cage}=\frac{v_{cage}}{(R+r)/2}=\frac{(\omega_{in}\times r)/2}{(R+r)/2}=\frac{\omega_{in}\times r}{(R+r)} \tag{14}$$

Because the inner-ring is fixed on rotor and rotates with shaft, $\omega_{in}=\omega_{rotor}$. When the number of rolling balls is N_b, VC frequency, namely, bearing ball passing frequency, can be expressed as

$$\omega_{VC}=\omega_{cage}\times N_b=\omega_{rotor}\times\left(\frac{r}{R+r}\times N_b\right)=\omega_{rotor}\times B_N \tag{15}$$

where B_N is the ratio of the VC frequency and the rotating frequency. Assume $\theta_j=\omega_{cage}\times t+2\pi/N_b(j-1),\quad j=1,2,\ldots,N_b$, in this expression, the variable θ_j represents the angle position of the jth rolling ball. When the vibration displacement of the inner-ring center in the X and Y directions are, respectively, assumed to be x and y, at the same time, bearing clearance is supposed to be $2r_0$; the normal contact deformation of the jth rolling ball and the raceway can be expressed as follows:

$$\delta_j=x\cos\theta_j+y\sin\theta_j-r_0 \tag{16}$$

The contact force F_j generated by the contact between the jth rolling ball and the raceway can be obtained by Hertzian theory. Since Hertzian contact can generate only positive forces, namely, the force is generated only when $\delta_j>0$, by using the Heaviside function H, the force can be written as

$$F_j=C_b[\delta_j]^{3/2}=C_b(x\cos\theta_j+y\sin\theta_j-r_0)^{3/2}\cdot H(x\cos\theta_j+y\sin\theta_j-r_0) \tag{17}$$

where C_b is the Hertz contact stiffness related to the shape and materials of contact objects. The components of F_j in the X and Y directions are

$$F_{jx}=F_j\cos\theta_j,\quad F_{jy}=F_j\sin\theta_j \tag{18}$$

Thus, bearing forces generated by the ball bearings are

$$F_x=\sum_{j=1}^{N_b}F_{jx}=\sum_{j=1}^{N_b}F_j\cos\theta_j,\quad F_y=\sum_{j=1}^{N_b}F_{jy}=\sum_{j=1}^{N_b}F_j\sin\theta_j \tag{19}$$

Therefore, we can obtain the bearing forces generated by the ball bearings in Fig. 4 as follows.

(1) When $x=x_r(L,t)-x_{wR}$, $y=y_r(L,t)-y_{wR}$, we can get $F_{xbR}=F_x$, $F_{ybR}=F_y$.
(2) When $x=x_r(0,t)-x_{wL}$, $y=y_r(0,t)-y_{wL}$, we can get $F_{xbL}=F_x$, $F_{ybL}=F_y$.

2.2.5 Squeeze Film Damping Force Model. Assume shaft journal length is L_J, shaft radius is R_J, oil film radius clearance is c, oil viscidity is μ, bearing center is O_B, journal center is O_J, journal eccentricity distance is e, eccentricity ratio is ε, and journal rotating angle is ϕ_J; on the assumption of short bearing, π film, and no end-sea, the oil film forces are

$$F_r=\frac{\mu R_J L_J^3}{c^2}\left[\frac{2\Omega_J\cdot\varepsilon^2}{(1-\varepsilon^2)^2}+\frac{\pi}{2}\cdot\frac{\dot\varepsilon(1+2\varepsilon^2)}{(1-\varepsilon^2)^{5/2}}\right]$$

$$F_t=\frac{\mu R_J L_J^3}{c^2}\left[\frac{\pi\Omega_J\cdot\varepsilon}{2(1-\varepsilon^2)^{3/2}}+\frac{2\varepsilon\dot\varepsilon}{(1-\varepsilon^2)^2}\right] \tag{20}$$

where

$$\varepsilon=e/c=\sqrt{x_J^2+y_J^2}/c,\quad \dot\varepsilon=\dot e/c=\frac{x_J\cdot\dot x_J+y_J\cdot\dot y_J}{c\sqrt{x_J^2+y_J^2}},$$

$$\varphi_J=\arctan\left(\frac{y_J}{x_J}\right),\quad \Omega_J=\dot\varphi_J=\frac{x_J\cdot\dot y_J-y_J\cdot\dot x_J}{x_J^2+y_J^2}$$

Therefore, in the XOY coordinate, the oil film forces are

$$F_x=F_r\cdot\cos\varphi_J-F_t\cdot\sin\varphi_J$$

$$F_y=F_t\cdot\cos\varphi_J+F_r\cdot\sin\varphi_J \tag{21}$$

In this paper, at the left (A) and right (B) bearings, the squeeze film dampers are considered.

(1) If $x_J=x_{wL}-x_{bL}$, $y_J=y_{wL}-y_{bL}$; $\dot x_J=\dot x_{wL}-\dot x_{bL}$, $\dot y_J=\dot y_{wL}-\dot y_{bL}$, then $F_{SFDxL}=F_x$, $F_{SFDyL}=F_y$.
(2) If $x_J=x_{wR}-x_{bR}$, $y_J=y_{wR}-y_{bR}$; $\dot x_J=\dot x_{wR}-\dot x_{bR}$, $\dot y_J=\dot y_{wR}-\dot y_{bR}$, then $F_{SFDxR}=F_x$, $F_{SFDyR}=F_y$.

2.2.6 Dynamic Equations of Bearing Outer-Rings. The following are the equations of the bearing outer-rings:

$$m_{wL}\ddot x_{wL}+k_{tLH}(x_{wL}-x_{bL})+c_{tLH}(\dot x_{wL}-\dot x_{bL})+F_{xbL}=0 \tag{22}$$

$$m_{wL}\ddot y_{wL}+k_{tLH}(y_{wL}-y_{bL})+c_{tLH}(\dot y_{wL}-\dot y_{bL})+F_{ybL}=-m_{wL}g \tag{23}$$

$$m_{wR}\ddot x_{wR}+k_{tRH}(x_{wR}-x_{bR})+c_{tRH}(\dot x_{wR}-\dot x_{bR})+F_{xbR}=0 \tag{24}$$

$$m_{wR}\ddot y_{wR}+k_{tRH}(y_{wR}-y_{bR})+c_{tRH}(\dot y_{wR}-\dot y_{bR})+F_{ybR}=-m_{wR}g \tag{25}$$

2.2.7 Dynamic Equations of Bearing Housings. The following are the equations of the bearing housings:

$$m_{bL}\ddot x_{bL}+k_{fLH}(x_{bL}-x_c)+c_{fLH}(\dot x_{bL}-\dot x_c)+k_{tLH}(x_{bL}-x_{wL})+c_{tLH}(\dot x_{bL}-\dot x_{wL})=0 \tag{26}$$

$$m_{bL}\ddot y_{bL}+k_{fLH}(y_{bL}-y_c)+c_{fLH}(\dot y_{bL}-\dot y_c)+k_{tLH}(y_{bL}-y_{wL})+c_{tLH}(\dot y_{bL}-\dot y_{wL})=-m_{bL}g \tag{27}$$

$$m_{bR}\ddot x_{bR}+k_{fRH}(x_{bR}-x_c)+c_{fRH}(\dot x_{bR}-\dot x_c)+k_{tRH}(x_{bR}-x_{wR})+c_{tRH}(\dot x_{bR}-\dot x_{wR})=0 \tag{28}$$

$$m_{bR}\ddot y_{bR}+k_{fRH}(y_{bR}-y_c)+c_{fRH}(\dot y_{bR}-\dot y_c)+k_{tRH}(y_{bR}-y_{wR})+c_{tRH}(\dot y_{bR}-\dot y_{wR})=-m_{bR}g \tag{29}$$

2.2.8 Dynamic Equations of Stator. The following are the equations of the stator:

$$m_c\ddot x_c+k_{cH}x_c+c_{cH}\dot x_c+k_{fRH}(x_c-x_{bR})+k_{fLH}(x_c-x_{bL})+c_{fRH}(\dot x_c-\dot x_{bR})+c_{fLH}(\dot x_c-\dot x_{bL})=-P_x \tag{30}$$

$$m_c\ddot y_c+k_{cH}y_c+c_{cH}\dot y_c+k_{fRH}(y_c-y_{bR})+k_{fLH}(y_c-y_{bL})+c_{fRH}(\dot y_c-\dot y_{bR})+c_{fLH}(\dot y_c-\dot y_{bL})=-P_y-m_cg \tag{31}$$

2.3 Calculation Parameters. The initial parameters of the rotor system are as follows: $E=2.07\times10^{11}$ Pa, $I=5.2\times10^{-8}$ m^4, $L=0.45$ m, $\rho A=1.543$ kg/m, the truncated mode number $NM=5$, $m_{rp}=14.059$ kg, $k_p=1.0\times10^9$ N/m, $c_p=1000$ N s/m, $m_{wL}=m_{wR}=2.0$ kg, $c_{rb}=1050$ N s/m, $e=0.01$ mm, $m_c=50$ kg, $m_{bL}=m_{bR}=10$ kg, $k_{fLH}=k_{fLV}=k_{fRH}=k_{fRV}=2.5\times10^8$ N/m, $c_{fLH}=c_{fLV}=c_{fRH}=c_{fRV}=2100$ N s/m, $k_{tLH}=k_{tLV}=k_{tRH}=k_{tRV}=2.5\times10^7$ N/m, $c_{tLH}=c_{tLV}=c_{tRH}=c_{tRV}=1050$ N s/m, $k_{cH}=k_{cV}=2.5\times10^9$ N/m, $c_{cH}=c_{cV}=2100$ N s/m, $k_r=2.5\times10^7$ N/m, $\delta=0.01$ mm, and $f=0.02$. Assume that the rotor disk is fixed on the rotating shaft, therefore, a very rigid connective stiffness and a relative strong damping are given, namely, $k_p=1.0\times10^9$ N/m

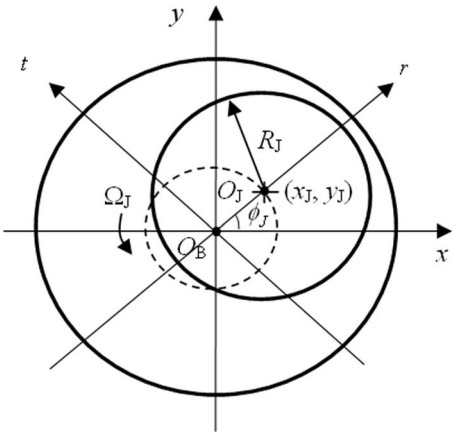

Fig. 5 SFD model

and $c_p = 1000$ N s/m.

In this paper, the JIS6306 ball bearing in literature [13] is adopted, and the SFDs at the left and right bearings are considered (see Fig. 5). The main parameters of the ball bearing and the SFD are shown in Table 2.

3 Dynamic Analysis for Rotor-Ball Bearing-Stator Coupling System

3.1 The New Type Fast Explicit Integration Method: Zhai Method. Because the rotor-ball bearing-stator coupling system belongs to the large-scale complicated system, and the Zhai method, which is a new type fast explicit integration method and put forward by Zhai in literature [14], is fit for solving large-scale complicated nonlinear system, in this paper the Zhai method is employed to obtain the system responses in this paper. The equations of system can be expressed as

$$[M]\{A\} + [C]\{V\} + [K]\{X\} = \{P\} \tag{32}$$

where $[M]$, $[C]$, and $[K]$ are the system inertia, damper, and stiffness matrices; $\{X\}$ is the system generalized displacement vector; $\{V\}$ is the system generalized velocity vector; $\{A\}$ is the system generalized acceleration vector; and $\{P\}$ is the system generalized force vector. The integration format is

$$\{X\}_{n+1} = \{X\}_n + \{V\}_n \Delta t + \left(\frac{1}{2} + \psi\right)\{A\}_n \Delta t^2 - \psi\{A\}_{n-1}\Delta t^2$$

$$\{V\}_{n+1} = \{V\}_n + \{1 + \phi\}\{A\}_n \Delta t - \phi\{A\}_{n-1}\Delta t \tag{33}$$

where Δt is the time step, subscript n denotes the moment $t = n\Delta t$, subscript $n+1$ denotes the moment $t = (n+1)\Delta t$, subscript $n-1$ denotes the moment $t = (n-1)\Delta t$, and ψ and ϕ are the integration parameters. In general, $\psi = \phi = 1/2$.

3.2 Varying Compliance Vibration Analysis for Ball Bearing. In Ref. [15], a dynamic model of an unbalanced rotor supported on ball bearings, which are subject to a constant vertical radial load, was established by Mevel and Guyader [15], and the sixth-order Runge–Kutta method was used to obtain the responses of the rotor. In this paper, the same ball bearing as reference is used, and the rotor responses of the rotor-ball bearing-stator coupling system are obtained by the Zhai method. Figure 6(*a*) shows the rotor disk vibration displacements in the *X* and *Y* directions at the rotating speed of 300 rpm in Ref. [15] by Mevel and Guyader; Fig. 6(*b*) shows the computation result of this paper. Obviously, their time waveforms and periods are very similar. Figure 6(*c*) shows the spectrum of Fig. 6(*b*).

The excitations of the unbalanced rotor, which supported on the ball bearing, come from two aspects: one is rotating frequency excitation from unbalance, and the other is the VC frequency excitation from the periodic variety of bearing stiffness. When the rotating speed is very low, unbalance force is very weak, and the VC vibration because of periodic variety of bearing stiffness can be observed clearly; hereinto, the frequency of VC vibration is *BN* times of rotating frequency; in this paper, the value of *BN* is 3.08 (according to Table 2). From Figs. 6(*a*) and 6(*b*), it can be seen that that the motions in the *X* and *Y* directions are periodic, and the ball passage frequency (VC frequency) is shown clearly. When a ball leaves the load zone, and the rotor falls and contacts the next ball, in this progress, the transient oscillations appear and disappear quickly. From the frequency spectrum of signals, as shown in Fig. 6(*c*), it can be seen that the rotor vibration represents the VC frequency (the ball passage frequency) and its multiple harmonic components. The study of Fukata et al. [13] shows that when the rotating speed is far from the two critical rotating speeds in the *X* and *Y* directions, the motion is periodic and represents the ball passage frequency and its multiple harmonic components. Apparently, the result of this paper accords with the conclusion.

Table 2 The main parameters of JIS6306 ball bearings and SFD

Outer-ring radius, R (mm)	Inner-ring radius, r (mm)	Ball No., N_b	Contact stiffness, C_b (N/m$^{3/2}$)	Clearance, $2r0$ (μm)	BN
63.9	40.1	8	13.34×10^9	10	3.08
Radius of journal, $2R$ (mm)	Loading length, L (mm)		Film diameter clearance, $2c$ (mm)	Viscidity, μ (Pa s)	
73.4	19.3		0.2	2.013×10^{-3}	

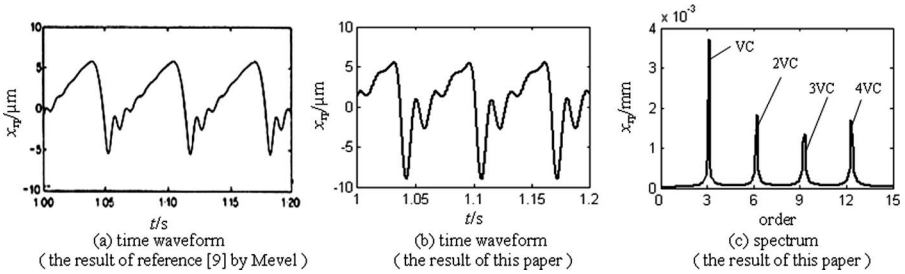

Fig. 6 The responses of rotor in the *X* direction (rotating speed is 300 rpm)

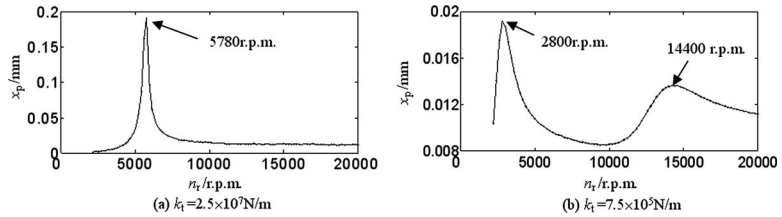

Fig. 7 Amplitude-rotating speed curves of rotor response under various support stiffnesses

3.3 Effect of Support on Rotor Dynamics Characteristics. The working speed of modern aero-engine is above 10,000 rpm in general, and the working speed of some small engines can even be up to 40,000–50,000 rpm. Therefore, it is essential to design rotor-support system and analyze its dynamic properties properly, and it is of the same importance to take necessary measures to reduce the rotor vibration. The main purposes of elastic support in rotor-support system are to (1) adjust and control the critical speed to meet the requirements of design criteria of rotor system, (2) change distribution of the strain energy of rotor-stator system to meet the requirements of design criteria, and (3) reduce the vibration through the deformation of elastic support to make damping work more effectively.

It is assumed that support stiffness is $k_{tLH}=k_{tLV}=k_{tRH}=k_{tRV}=k_t$; in order to simplify problem, the SFD is taken as linear viscous damping, namely, $c_{tLH}=c_{tLV}=c_{tRH}=c_{tRV}=1050$ N s/m. The responses of rotor with various support stiffnesses are obtained by means of numerical simulation, and the amplitude-rotating speed curves of rotor response under various support stiffnesses are shown in Fig. 8, in which the amplitudes of steady-state response in each speed are given and where *X*-axis and *Y*-axis, respectively, denote rotating speed and amplitude. Rotating shaft vibration modal is normalized according to the left end of shaft vibration displacement.

that the following can be found from Fig. 7: (1) For a support stiffness $k_t=2.5\times10^7$ N/m, there is no rotor rigid motion, only a resonance peak appears in the rotor response, and it corresponds to the first-order bending transverse natural frequency of rotor, that is, the first order of rotor critical speeds (5780 rpm), as shown in Fig. 7(*a*). The vibration modal at the critical speed is shown in Fig. 8(*a*), from which it can be seen that there is a great bending deformation of the rotor. (2) For flexible support $k_t=7.5\times10^5$ N/m, it can be seen in Fig. 7(*b*) that there are two resonance peaks that, respectively, correspond to two critical speeds, the lower of which corresponds to the speed of rigid motion and the higher of which corresponds to the first-order bending critical speed. The vibration modal at the lower critical speed is shown in Fig. 8(*b*) and the one at the higher critical speed is shown in Fig. 8(*c*). (3) It can be easily seen that the bending critical speed under lower stiffness support (corresponding to the second critical speed, $n_{cr2}=14,400$ rpm) is up to 2.49 times of the first-order bending critical speed under rigid support ($n_{cr1}=5785$ rpm). (4) At the same time, comparing the responses of rotor with different support stiffnesses, we can find that the amplitude for resonance response under low stiffness support is much smaller than the one under high stiffness support. It is proved that using low stiffness support cannot only effectively change the rotor bending critical speed but also effectively reduce the rotor vibration at the critical speed through producing bigger deformation to increase the damping effect. This characteristic is clearly indicated by the simulated results in this paper.

3.4 Effect of Truncated Modal Number on the Rotor Responses. It is known from formulas (3) and (8) that the vibration responses of shaft can be approximated by truncating limited low-order modes; therefore, the effect of truncated modal number *NM* on rotor needs to be analyzed. The above calculations indicate that, when the support stiffness $k_t=2.5\times10^7$ N/m, the first-order bending critical speed of rotor is $n_r=5780$ rpm; when the support stiffness $k_t=7.5\times10^5$ N/m, the first-order bending critical speed of rotor is $n_r=14,400$ rpm. In this paper, on the conditions of different truncated modal numbers *NM*, the mean square values (MSVs) of the response displacement, and the velocity and acceleration of rotor disk at different critical speeds are shown in Fig.

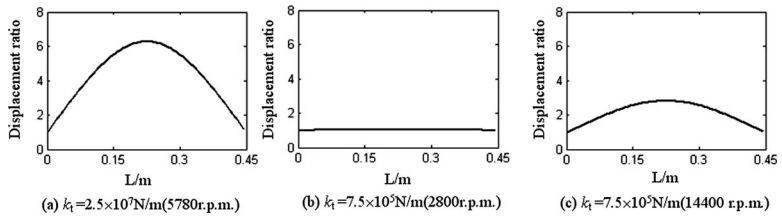

Fig. 8 Vibration modes of rotor response at critical speed under various support stiffnesses

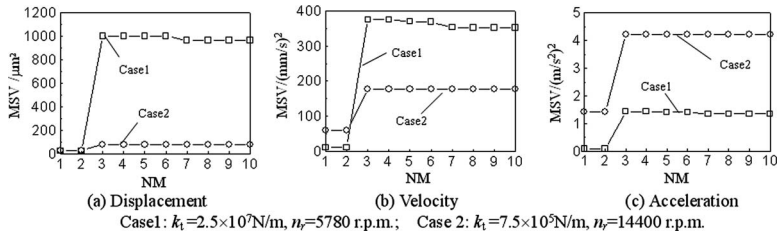

Fig. 9 The effect of cutting mode number on the rotor responses

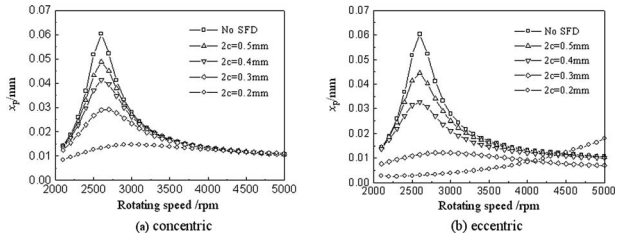

Fig. 10 Effect of SFD on rotor vibration response

9. As to the free beam, the first two modals are rigid vibration modals and the third one is bending vibration modal. From Fig. 8 it can be known that, when $NM \geq 3$, the responses are enough accurate; in general, too much truncated mode number NM will increase the number of equations and require a smaller integral step; all of these will greatly increase the computation load. Clearly, the truncated mode number $NM=5$ in this paper is relatively appropriate.

3.5 Effect of SFD on Rotor Movement Characteristics. The function of SFD is to decrease the amplitude during passing the resonance region. Currently, modern aero-engine widely uses SFD to reduce vibration in design. In this paper, the SFDs are installed at the left and right bearings, the rotor responses near 1-order critical rotating speed under support stiffness $k_t=7.5\times10^5$ N/m are simulated, and the responses under different film diameters of SFD and concentric degrees are also simulated. In this paper, the elastic support is assured concentric with damper outer-ring by means of adding an "eccentricity distance" to journal. For the rotor parameters of this paper, the "eccentricity distance" is 0.12 mm; however, if the eccentricity distance is 0, because of rotor gravity, the eccentricity will appear.

Figures 10(*a*) and 10(*b*) show the amplitude-speed curves under different concentric degrees and different oil film diameters. Comparing Figs. 10(*a*) and 10(*b*), the following conclusions can be drawn: (1) The smaller the SFD oil film diameter is, the better is the reducing vibration effect. (2) Under eccentricity, the squeezing force is greater, and the reducing vibration effect is better. However, the eccentricity will lead to other design problems such as rubbing between journal and bearing housing, the elastic support fatigue damage, and so on. In design, the measurements should be adopted to make the shaft journal concentric with the bearing housing.

3.6 Transient Response Analysis of Blade Loss. Aero-engine design prescribe that the rotor system transient responses of blade loss must be analyzed in order to confirm if the design of the SFD can absorb rotor vibration energy and decrease the sensibility to unbalance. In this paper, the concentric SFDs are set at the left and right bearings. Assuming that the sudden-adding imbalance after blade loss is 100 g cm, the original imbalance of the rotor system is 14 g cm, the rotating speed is 10,000 rpm, and the elastic support stiffness $k_t=7.5\times10^5$ N/m. Figures 11 and 12 show, respectively, the journal orbits of left bearing A, the journal displacement of bearing A in the X direction, and the velocity of stator in the X direction on the conditions of the SFD film diameters $2c=0.3$ mm and $2c=0.2$ mm.

Simulation results show that the transient process is very impermanent and the vibration can stabilize on the new level. In addition, from the simulation results, it can be found that the small SFD film diameter has better reducing vibration effect.

3.7 Dynamic Characteristic Analysis for Rub-Impact Faults. In this paper, the rubbing fault responses are obtained through numerical simulation; the computation conditions are as follows: rubbing stiffness $k_r=2.5\times10^7$ N/m, eccentricity distance $e=0.01$ mm, rotor-stator clearance is 0.01 mm, friction coefficient $f=0.02$, and the rotor disk is assured centric with the stator through adjusting the rotor disk position. Figures 13(*a*)–13(*d*) show, respectively, the waterfall plots of the rotor disk responses in the X direction on the conditions of support stiffnesses $k_t=7.5\times10^5$ N/m and $k_t=2.5\times10^7$ N/m, and oil film diameters $2c=0.2$ mm and $2c=0.3$ mm. Figures 14(*a*)–14(*d*) show, respectively, the corresponding system bifurcation plots at the high rotating speed regions.

From Figs. 13 and 14, the following conclusions can be drawn: (1) It can be found that in the speed region under critical speed there are abundant superharmonics in which the second harmonic is dominant, and the subharmonics are not obvious. In the speed range over critical speed, subharmonics appear, but the superharmonics are not obvious. (2) Smaller SFD will produce stronger damping force, and the reducing vibration effect is better, and the probability of generating frequency division, quasiperiodicity, and

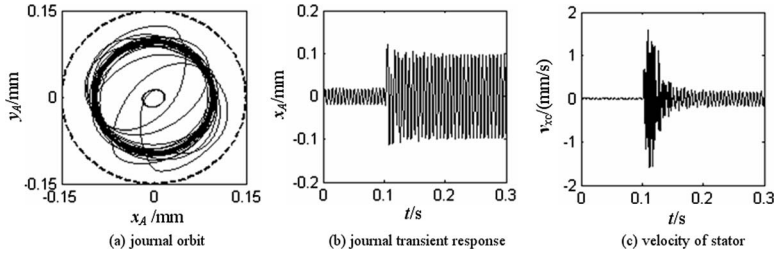

Fig. 11 Transit response after sudden-adding unbalance ($2c=0.3$ mm)

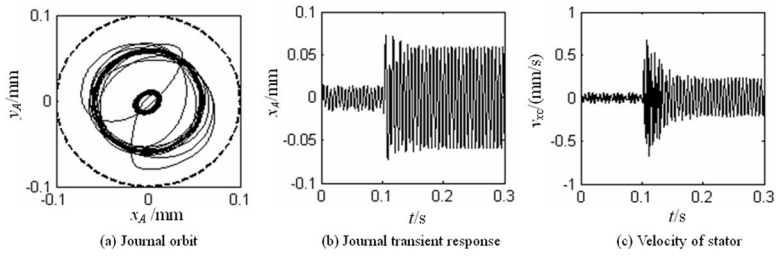

Fig. 12 Transit response after sudden-adding unbalance ($2c=0.2$ mm)

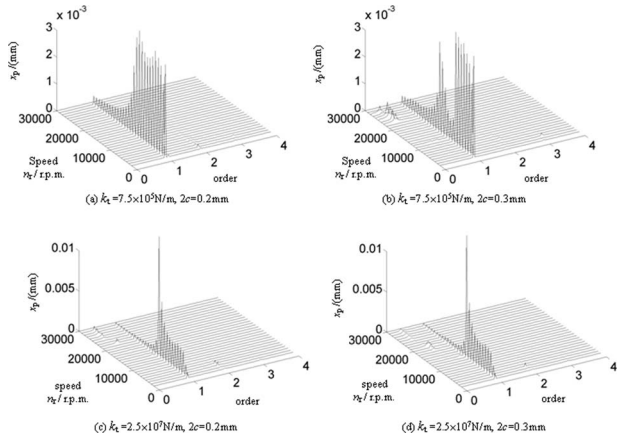

Fig. 13 Waterfall plots of rotor responses

chaos movement is greatly decreased. (3) Under the low stiffness support, the support elastic deformation is bigger, the squeezing effect of journal to the oil film is stronger, damping force increases, and the reducing vibration effect is better. Therefore, on the condition of the same oil film diameter, the lower stiffness elastic support will generate less frequency division, quasiperiodicity, and chaos movement.

4 Experimental Verification and Analysis

In order to simulate the rotor vibration of the real aero-engine, an aero-engine rotor tester is designed and manufactured. By comparison with the real aero-engine, the tester has the following features: (1) Its size is one-third of the real aero-engine and its shape is similar to the stator of engine; (2) its internal structure is simplified: the core machine is simplified as a rotor with two disks, which are, respectively, turbine disk and compressor disk, and the support stiffness is adjustable in order to adjust the dynamic characteristics of the system; multistage compressor is simplified as a single-stage disk structure; compressor blade is simplified as the inclined plane shape; (3) its shaft is solid and rigid and its maximal rotating speed is 7000 rpm; and (4) the rotor is driven by motor, and the flame tube is canceled. Therefore, the aero-engine rotor tester becomes a single-rotor system model, and its real photo is shown in Fig. 15(*a*) and its section drawing is shown in Fig. 15(*b*).

The rotor tester is driven by an electromotor. Considering that the electromotor shaft is difficult to keep its alignment with the

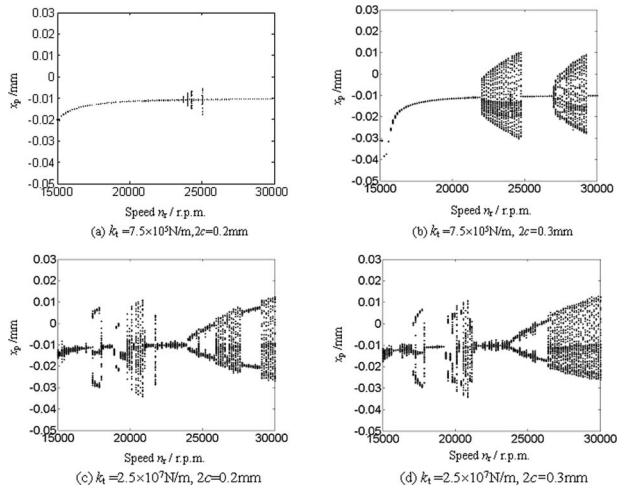

Fig. 14 Bifurcation plots of rotor responses

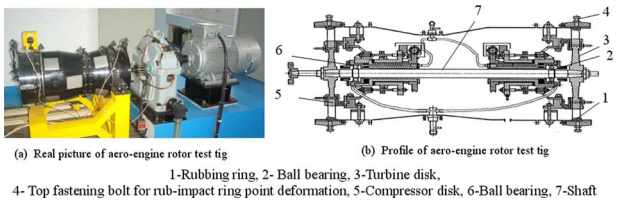

Fig. 15 Aero-engine rotor rig

shaft of the rotor tester, a soft connection is adopted between the two shafts. The vibration testing system of the aero-engine rotor tester is shown in Fig. 16. The rotating speed can be obtained by way of detecting the pulse number of the eddy current transducer, which is installed at testing point ①, and the rotor fault signals in the X and Y directions are picked up, respectively, by four eddy current transducers, which are installed at testing points ② and ③. The fault analog signal is enlarged by a preamplifier first, and then is sampled and quantified into digital signals by the USB-14054 data acquisition instrument, finally the digital signal is sent into a PC.

Aero-engine rubbing experiment is shown in Fig. 17. First, make engine operate at a certain speed, and then to wire rub-impact screw "1" with wrench "5" in order to make rubbing ring generate deformation and rub with rotating turbine blades. When rubbing is very serious, rubbing sparks "2" will appear. The vibration displacements of shaft are picked up by eddy current displacement sensors in X direction "4" and in Y direction "3."

The waterfall plot of response of rotor with coupling faults of imbalance and rubbing is obtained by the new rotor-ball bearing-stator coupling system dynamics model in this paper and it is shown in Fig. 18(*a*); the computation conditions are as follows: rubbing clearance $\delta=0.02$, rubbing stiffness $k_r=2.5\times10^7$ N/m, friction coefficient $f=0.02$, and $k_{tLH}=k_{tLV}=k_{tRH}=k_{tRV}=k_t=7.5\times10^5$ N/m; because there are no SFDs in the aero-engine rotor tester, in the simulation computation, the SFDs are considered as linear viscous damping, namely, $c_{tLH}=c_{tLV}=c_{tRH}=c_{tRV}=c_t=1050$ N s/m. The response waterfall plot of the rotor obtained by rub-impact experiments with an aero-engine rotor test rig is shown in Fig. 18(*b*).

By comparison between Figs. 18(*a*) and 18(*b*), it can be seen that both of the results from simulations and experiments all re-

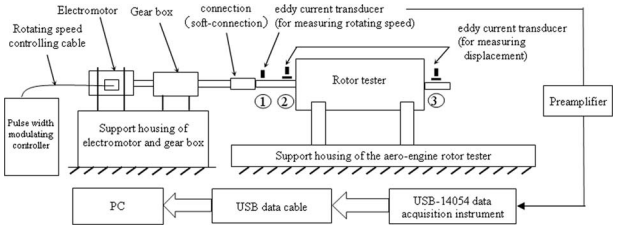

Fig. 16 The vibration testing system of the aero-engine rotor tester

1-rub-impact screw; 2-rubbing sparks; 3-displacement sensor in Y direction; 4-displacement sensor in X direction; 5-rubbing resulted from wiring screw

Fig. 17 Aero-engine rotor rubbing experiment

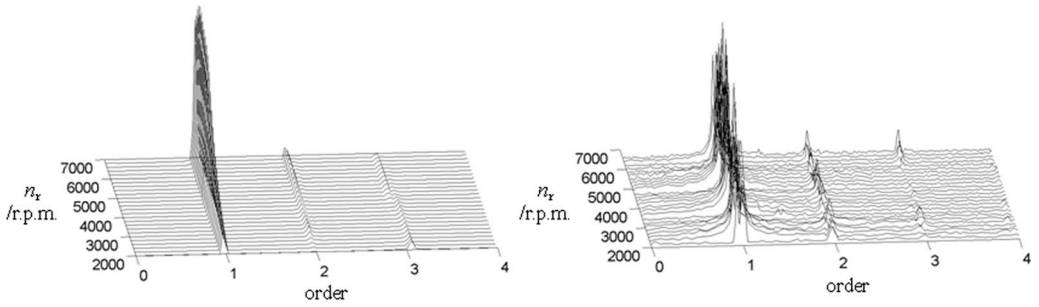

Fig. 18 The simulation and experimental waterfall plots of rotor responses

flect superharmonics such as the second harmonic and the third harmonic resulted from rubbing faults. Because the speed of the test rig is only up to 7000 rpm, which means that it can only work under critical speed, the frequency division and chaos phenomena cannot be observed, which is shown by simulation and experimental results. The qualitative consistency of simulation and experimental results to some extent verifies the correctness of the new rotor-ball bearing-stator coupling model in this paper.

5 Conclusions

A rotor-ball bearing-stator coupling system dynamics model for whole aero-engine vibration is established, in which the rotor is considered as an Euler free beam model with equal-section, and rotor dynamics analysis is done by truncating limited modals; in the ball model, the VC vibration resulted from changes in the rolling bearing stiffness, and Hertz nonlinear contact force and bearing clearance are all taken full account into; in the rotor system with faults, the imbalances and rub-impact faults are fully considered. The dynamic equations of coupling system are deduced and Zhai method is used to solve the equations.

The ball bearing VC vibration characteristics are studied through numerical simulation, and the results are compared with the known researches, and the correction of the new model is verified. In addition, the effect of rotating shaft truncated modal number on vibration response is studied.

Through computer simulation it can be found that elastic support cannot only effectively change the rotor critical speed, but also reduce the rotor vibration at the critical speed effectively through increasing damping effect due to bigger elastic deformation. This simulation result is in conformity with the whole machine vibration characteristics of practical aero-engine.

It can be found that under the critical speed, rubbing will generate many superharmonics in which the second harmonic is greater; above the critical speed, a lot of fractional harmonic will be resulted from rubbing faults. At the same time, superharmonic, subharmonic, quasiperiod, and chaos generated by rubbing faults will be greatly reduced with lower support stiffness and smaller SFD film diameter.

The aero-engine rotor test rig is designed and manufactured, and the rubbing fault experiments are done. The qualitative consistency of simulation and experimental results also to a certain extent verifies the correctness for the new rotor-ball bearing-stator coupling system dynamics model in this paper.

The researches in this paper provide a new method and idea for further study on the nonlinear dynamics response characteristics of the complicated rotor-ball bearing-stator coupling system of real aero-engine and the feature extractions for coupling faults of rotor and rolling bearing.

Acknowledgment

The author is very grateful to his master graduate student M.L. Wang, who helped in the translation and data collection work for this paper. The work is supported by the National Science Foundation of China (Grant No. 50705042) and the Aviation Science Funds of China (Grant No. 2007ZB52022).

References

[1] Muszynska, A., 1989, "Rotor-to-Stationary Element Rub-Related Vibration Phenomena in Rotating Machinery," Shock Vib. Dig., **21**, pp. 3–11.
[2] Zhang, Y. M., Wen, B. C., and Liu, A. L., 2003, "Reliability Sensitivity for Rotor-Stator Systems With Rubbing," J. Sound Vib., **259**(5), pp. 1095–1107.
[3] Muszynska, A., and Goldman, P., 1995, "Chaotic Responses of Unbalance Rotor Bearing Stator Systems With Looseness or Rubs," Chaos, Solitons Fractals, **5**(9), pp. 1683–1704.
[4] Wen, B. C., Wu, X. H., and Han, Q. K., 2004, *The Nonlinear Dynamics Theory and Experiments of Rotating Mechanism With Faults*, Science, Beijing, China, pp. 1–10, in Chinese.
[5] Liew, A., Feng, N., and Hahn, E. J., 2002, "Transient Rotordynamic Modeling of Rolling Element Bearing Systems," ASME J. Eng. Gas Turbines Power, **124**, pp. 984–991.
[6] Jang, G. H., and Jeong, S. W., 2002, "Nonlinear Excitation Model of Ball Bearing Waviness in a Rigid Rotor Supported by Two or More Ball Bearings Considering Five Degrees of Freedom," ASME J. Tribol., **124**, pp. 82–90.
[7] Bai, C. H., and Xu, Q. Y., 2006, "Dynamic Model of Ball Bearings With Internal Clearance and Waviness," J. Sound Vib., **294**, pp. 23–48.
[8] Chen, G., Li, C. G., and Wang, D. Y., 2008, "Nonlinear Dynamic Analysis and Experiment Verification of Rubbing Faults of Rotor-Ball Bearing-Support-Stator Coupling System for Aero-Engine," Journal of Aerospace Power, **23**(7), pp. 1304–1311.
[9] Hai, P. M., and Bonello, P., 2008, "An Impulsive Receptance Technique for the Time Domain Computation of the Vibration of a Whole Aero-Engine Model With Nonlinear Bearings," J. Sound Vib., **318**, pp. 592–605.
[10] Sun, G., Palazzolo, A., Provenza, A., Lawrence, C., and Carney, K., 2008, "Long Duration Blade Loss Simulations Including Thermal Growths Dual-Rotor Gas Turbine Engine," J. Sound Vib., **316**, pp. 147–163.
[11] Petyt, M., 1998, *Introduction to Finite Element Vibration Analysis*, Cambridge University Press, Cambridge.
[12] Cao, Z. Y., 1989, *The Vibration Theory of Plate and Shell*, China Railway, Beijing, China, in Chinese.
[13] Fukata, S., Gad, E. H., and Kondou, T., 1985, "On the Radial Vibration of Ball Bearings (Computer Simulation)," Bull. JSME, **28**, pp. 899–904.
[14] Zhai, W. M., 1996, "Two Simple Fast Integration Methods for Large-Scale Dynamic Problems in Engineering," Int. J. Numer. Methods Eng., **39**(24), pp. 4199–4214.
[15] Mevel, B., and Guyader, J. L., 1993, "Routes to Chaos in Ball Bearings," J. Sound Vib., **162**(3), pp. 471–487.